Digital Object Identifier 10.1109/PEDG56097.2023.10215196

IEEE 14th International Symposium on Power Electronics for Distributed Generation Systems (PEDG)

Stability Comparison of Grid-Forming Converters with Different Power Calculation Strategies

Ziqi Zhou
Sante Pugliese
Marco Liserre

Suggested Citation

Z. Zhou, S. Pugliese and M. Liserre, "Stability Comparison of Grid-Forming Converters with Different Power Calculation Strategies," 2023 IEEE 14th International Symposium on Power Electronics for Distributed Generation Systems (PEDG), Shanghai, China, 2023, pp. 800-805

2023 IEEE 14th International Symposium on Power Electronics for Distributed Generation Systems (PEDG) | 979-8-3503-2823-3/23/$31.00 ©2023 IEEE | DOI: 10.1109/PEDG56097.2023.10215196

Stability Comparison of Grid-Forming Converters with Different Power Calculation Strategies

Ziqi Zhou
Chair of Power Electronics.
Kiel University.
Kiel, Germany
ziqi@tf.uni-kiel.de

Sante Pugliese
Chair of Power Electronics.
Kiel University.
Kiel, Germany
sapu@tf.uni-kiel.de

Marco Liserre
Chair of Power Electronics.
Kiel University.
Kiel, Germany
ml@tf.uni-kiel.de

***Abstract*—Grid-forming (GFM) converters, such as virtual synchronous generators (VSGs), behave as voltage sources behind a reactance within a specified frequency range. Therefore, solutions to limit the rapid growth of the converter output current, which may cause over-current tripping during grid faults, are necessary. One effective solution is to use outer dual-loop voltage and current control so that current limitation can be realized by saturating the current reference. In the condition, electrical power (EP) of VSG can be calculated either with the converter output current or with the virtual current from the voltage loop, leading to different small-signal stability for the GFM converter. In this paper, small-signal stability of these two EP calculation methods are analysed and compared. Small-signal eigenvalues analysis shows that using virtual current from outer voltage loop for EP calculation contributes to better small-signal stability as compared to the conventional EP calculation approach, under both the weak grid and the strong grid conditions. Simulation results are provided to validate the effectiveness of the analysis.**

***Index Terms*—Grid-forming, Current Control, Virtual Admittance, Stability Analysis, Current limiting**

I. Introduction

The renewable energy generation systems (REGS) are integrated into the electrical grid through power electronics based grid-side-converters. Generally, control methods applied to the converter can be roughly classified into two types, i.e., grid-following (GFL) mode and grid-forming (GFM) mode [1]. The GFL converters have been widely used in REGS such as solar farm and wind farm. However, GFL converters are generally considered to provide no inertia to the power system, thus challenging the stability of the power system as the penetration of GFL converter gradually goes up. Besides, GFL converters need a synchronization unit such as phase-lock-loop (PLL) to track the point of common coupling (PCC) voltage, making itself susceptible to the dynamic of the PCC voltage under weak-grid condition [2]. Due to the requirement of external synchronization unit, islanded operation is also a big challenge for GFL converters. Nevertheless, GFL converter performs good current limitation during grid events since it behaves as a current source.

Differently from GFL converters, GFM converters do not need a synchronization unit and can realize self-synchronization through various control methods such as synchronverter [3]. The principle of VSG is to emulate the swing equation of a real synchronous machine. Therefore, VSG provides inertia and frequency support to the grid during grid events, thus improving the stability of the power system [4]. Moreover, VSG performs as a voltage source behind an impedance, which makes it much more suitable for connection under weak-grid conditions. However, rush output currents might be generated by GFM converters during large grid faults and the small-signal stability of the GFM converter under strong-grid conditions is challenged.

To avoid over-current issues under grid faults, many methods have been proposed in literatures and reviewed in [5]. One of the methods is to implement an inner current loop to limit the current, and outer voltage loop to regulate the voltage across the filter capacitor [6]. In this condition, the current limitation can be realized by saturating the reference of the inner current loop during a fault. However, EP of a GFM converter is generally calculated with the converter output current. Therefore, the maximum value of EP is also limited due to the current limitation approach. This may leads to the imbalance between the mechanical power (MP) and EP during the fault, causing transient stability problems [7].

Instead of using the real converter output current, [8] came up with a novel VSG control which uses virtual current from the voltage loop to calculate EP. In this condition, balance between the MP and EP during the fault can be realized, because EP is independent from the actual converter current. Therefore, better transient stability under grid fault could be realized as compared to the conventional VSG using output current for power calculation. Nevertheless, the small-signal stability comparison between these two power calculation methods are not discussed in details.

In this paper, small-signal eigenvalues analysis is used to evaluate and compare the stability of the GFM converter with two different EP calculation methods. The rest of the paper is organized as follow: Section II introduces the main circuit and control structure of the studied GFM converter with voltage and current dual-loop control and two different EP calculation methods. In Section III, the small-signal stability of two methods is analyzed. Section IV provides simulation results to verify the small-signal analysis and the synchronization stability of two methods. Section V concludes the paper.

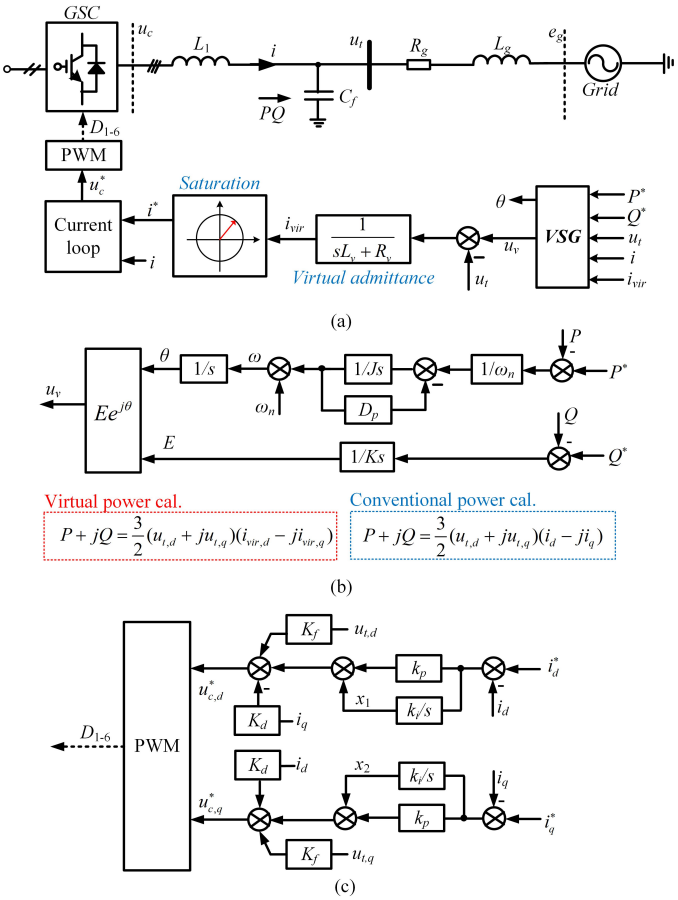

Fig. 1. Main circuit and control structures of the GFM converter. (a) Main circuit and control diagram. (b) Control algorithm for VSG with two different power calculation methods. (c) Control algorithm for the current loop.

II. Main Circuit and Control Structures of the GFM Converter

Fig.1 (a) shows the main circuit in one phase and the control diagrams of the studied GFM converter grid-connected system. In the figure, e_g, u_t and u_c are the grid voltage, PCC voltage and the converter output voltage, respectively; i and i_g are the converter output current and the grid current, respectively; P and Q represent for the calculated output power of the GFM converter; P^* and Q^* represent for the GFM power reference; L_1 and L_g are the converter filter inductance and the grid inductance, respectively; R_g is the resistance on the grid impedance; C_f is the filter capacitance.

The GFM control implementation can be divided by three parts: VSG, voltage loop and current loop. The VSG realizes power synchronization with the grid by emulating the swing equation of a synchronous generator (SG), as shown in Fig.1 (b). In the figure, u_v is the output voltage of the VSG; J is the virtual inertia of the VSG while D_p is the damping coefficient; ω_n and ω are the fundamental frequency and the VSG frequency, respectively; K is the integral gain for the VSG reactive power loop; E voltage magnitude of the u_v; θ is the angle of the VSG and is taken as the reference for abc-dq transformation. The VSG power PQ is generally calculated through the actual PCC voltage u_t and the actual converter current i, expressed as

$$P + jQ = \frac{3}{2}(u_{t,d} + ju_{t,q})(i_d - ji_q). \tag{1}$$

To improve synchronization stability during the grid fault, the converter current i is replaced by the virtual current i_{vir} for virtual power calculation. In this condition, the VSG power is rewritten as

$$P_{vir} + jQ_{vir} = \frac{3}{2}(u_{t,d} + ju_{t,q})(i_{vir,d} - ji_{vir,q}). \tag{2}$$

The values of virtual current i_{vir} are generated through the outer voltage loop which is realized by a virtual admittance block, expressed as:

$$i_{vir,abc} = \frac{u_{v,abc} - u_{t,abc}}{sL_v + R_v}. \tag{3}$$

In (3), L_v and R_v are the equivalent stator impedance of a synchronous generator while subscript 'abc' denote for corresponding variables in three phases. Besides, power calculation through (1) is denoted as conventional power method while power calculation through (2) is denoted as virtual power method in this paper.

i_{vir} are then limited to i^* through the saturating block to avoid the over-current condition during the grid fault. The detailed algorithm of the saturating block varies according to different requirements in the practice. Finally, i^* is taken as the current reference of the current loop to regulate the converter output current i, as shown in Fig.1 (c). The current loop uses PI controller to track i^* and k_p and k_i are the proportional gain and the integral gain of the PI controller, respectively. Besides, K_f is the the PCC voltage feed-forward coefficient while K_d is the crossing decoupling coefficient.

When the saturating block is not activated and the system is operating in the steady state, it can obtain:

$$i_{vir} = i^* = i, \tag{4}$$

indicating that different power calculation methods in (1) and (2) will not affect the power regulation accuracy.

On this basis, small-signal stability of the GFM converter with two power calculation methods are quantitatively analyzed in the next Section.

III. Stability Comparison of Two Power Calculation Methods

A. Small-Signal State-Space Modeling

In this Section, small-signal differential equations of the GFM converter grid-connected system shown in Fig.1 are derived. Since the GFM converter grid-connected system consists of the electrical circuit and the digital control part, two rotating frames are considered for the small-signal analysis, i.e., the xy frame which synchronizes with the grid voltage e_g and the dq frame which synchronizes with the VSG voltage u_v, shown in Fig.2. In the figure, ω_g is the frequency of e_g and it has ω_g=ω in the steady state. Following assumptions are considered to

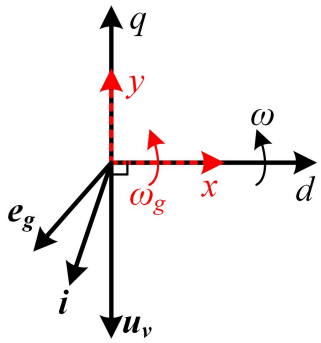

(a)

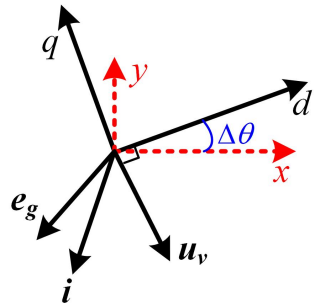

(b)

Fig. 2. Phasor diagrams of the xy frame and the dq frame. (a) Steady state. (b) Transient state under a small-signal disturbance.

simplify the analysis:

1. Grid voltage e_g is considered to be stiff;
2. xy frame and the dq frame are in the same phase in the steady state;
3. Digital delay of the control system is neglected.

With the assumptions, it is intuitive that the frequency of the xy frame keeps unchanged while the rotational frequency of the dq frame will respond to the small-signal disturbance in the system, leading to a phase difference $\Delta\theta$ between the two frames, shown in Fig.2 (b) .

Besides, the subscript '0' denotes a steady-state operating point; Subscript 'dq' denote for corresponding variables in dq frame; Subscript 'xy' denote for corresponding variables in xy frame; The symbol 'Δ' denotes a small-signal perturbation of a variable.

On the basis, the small-signal differential equations of the main circuit in xy frame can be derived by [9]:

$$\begin{cases} \Delta u_{t,x} - \Delta e_{g,x} = L_g \frac{d\Delta i_{g,x}}{dt} - \omega_n L_g \Delta i_{g,y} + R_g \Delta i_{g,x} \\ \Delta u_{t,y} - \Delta e_{g,y} = L_g \frac{d\Delta i_{g,y}}{dt} + \omega_n L_g \Delta i_{g,x} + R_g \Delta i_{g,y} \end{cases}. \tag{5}$$

$$\begin{cases} C_s \frac{d\Delta u_{t,x}}{dt} - \omega_n C_s \Delta u_{t,y} = \Delta i_x - \Delta i_{g,x} \\ C_s \frac{d\Delta u_{t,y}}{dt} + \omega_n C_s \Delta u_{t,x} = \Delta i_y - \Delta i_{g,y} \end{cases}. \tag{6}$$

$$\begin{cases} \Delta u_{c,x} - \Delta u_{t,x} = L_1 \frac{d\Delta i_x}{dt} - \omega_n L_1 \Delta i_y \\ \Delta u_{c,y} - \Delta u_{t,y} = L_1 \frac{d\Delta i_y}{dt} + \omega_n L_1 \Delta i_x \end{cases}. \tag{7}$$

According to the Park transformation and the Inverse-Park transformation, the coordinate transformation between the xy frame and the dq frame can be given as:

$$\begin{cases} \Delta u_{t,d} = \Delta u_{t,x} + u_{t,y0} \Delta\theta \\ \Delta u_{t,q} = \Delta u_{t,y} - u_{t,x0} \Delta\theta \end{cases}. \tag{8}$$

$$\begin{cases} \Delta i_d = \Delta i_x + i_{y0} \Delta\theta \\ \Delta i_q = \Delta i_y - i_{x0} \Delta\theta \end{cases}. \tag{9}$$

$$\begin{cases} \Delta u_{c,x} = \Delta u_{c,d} - u_{c,q0} \Delta\theta \\ \Delta u_{c,y} = \Delta u_{c,q} + u_{c,d0} \Delta\theta \end{cases}. \tag{10}$$

Then the small-signal linearized equations of the virtual admittance block can be derived by:

$$\begin{cases} L_v \frac{d\Delta i_{vir,d}}{dt} - \omega_n L_v \Delta i_{vir,q} + R_v \Delta i_{vir,d} = \Delta u_{v,d} - \Delta u_{t,d} \\ L_v \frac{d\Delta i_{vir,q}}{dt} + \omega_n L_v \Delta i_{vir,d} + R_v \Delta i_{vir,q} = \Delta u_{v,q} - \Delta u_{t,q} \end{cases}, \tag{11}$$

where $u_{v,q} = -E$ and $u_{v,d} = 0$ in the steady state. Besides, the small-signal linearized equations of the current loop are given by:

$$\begin{cases} \frac{d\Delta x_1}{dt} = k_i(\Delta i_{vir,d} - \Delta i_d) \\ \frac{d\Delta x_2}{dt} = k_i(\Delta i_{vir,q} - \Delta i_q) \end{cases}, \tag{12}$$

$$\begin{cases} \Delta u_{c,d} = K_f \Delta u_{t,d} - K_d \Delta i_q + \Delta x_1 + k_p(\Delta i_{vir,d} - \Delta i_d) \\ \Delta u_{c,q} = K_f \Delta u_{t,q} + K_d \Delta i_d + \Delta x_2 + k_p(\Delta i_{vir,q} - \Delta i_q) \end{cases}, \tag{13}$$

where x_1 and x_2 are the output of the integrator of the PI controllers. Moreover, the small-signal linearized equations of the swing equation are given by:

$$\begin{cases} \frac{d\Delta\theta}{dt} = \Delta\omega \\ \frac{d\Delta\omega}{dt} = \frac{1}{J\omega_n}(\Delta P^* - \Delta P) - \frac{D_p}{J}\Delta\omega \end{cases}. \tag{14}$$

The small-signal linearized equation of the reactive power loop is given by:

$$\frac{d\Delta E}{dt} = \frac{1}{K}(\Delta Q^* - \Delta Q). \tag{15}$$

According to (1), (2), (8) and (9), the small-signal linearized equations of the active power and reactive power calculated by the conventional power method or the virtual power method can be derived by (A.1) and (A.2) respectively, shown in the Appendix.

Finally, according to (5)-(15), (A.1) and (A.2), the state-space model of the GFM converter grid-connected system can be derived as:

$$\mathbf{\Delta\dot{x}_{n(13\times1)}} = \mathbf{A_{n(13\times13)}} \cdot \mathbf{\Delta x_{n(13\times1)}} + \mathbf{B_n} \cdot \mathbf{\Delta u_n}. \tag{16}$$

In (16), n = 1,2 represent for the corresponding matrix under the conventional power method or the virtual power method, respectively. Since the stability of the system only depends of the state-space matrix $\mathbf{A_n}$, only matrixes of $\mathbf{A_n}$ are shown in the Appendix.

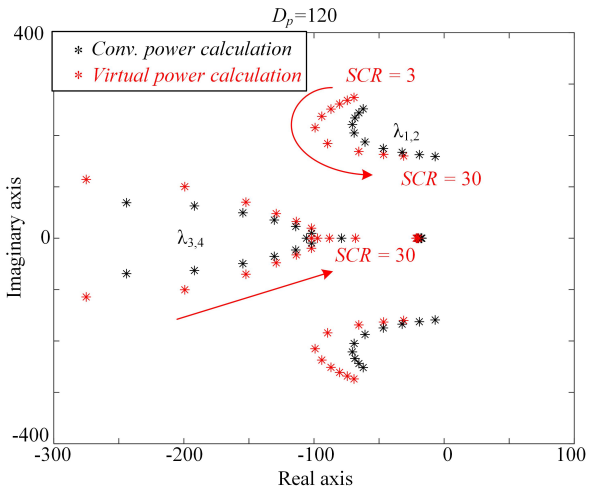

Fig. 3. Eigenvalues of the GFM converter under different SCR when D_p=120.

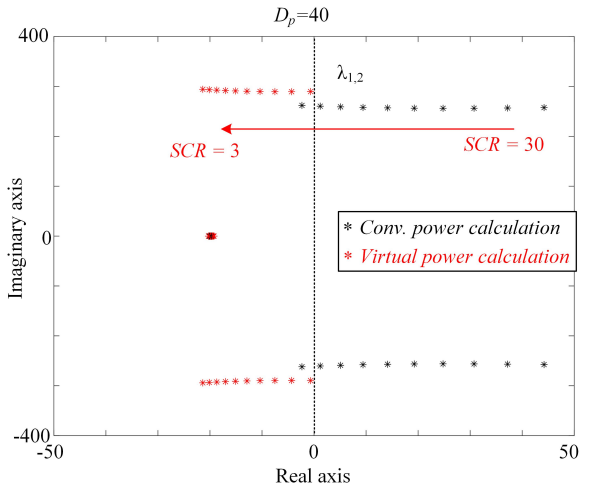

Fig. 4. Eigenvalues of the GFM converter under different SCR when D_p=40.

B. Small-signal stability analysis

System and control parameters of a 1MW GFM converter are shown in Table I. With the various grid impedance given in the Table, the short circuit ration (SCR) of the system will vary from 3 to 30. On this basis, Fig.3 shows the dominant eigenvalues near the imaginary axis under difference power calculation methods, where different SCR is used to evaluate the stability of the system.

In Fig.3, trajectories of two pairs of dominant eigenvalues are highly affected by the change of SCR, i.e., mode $\lambda_{1,2}$ and the mode $\lambda_{3,4}$. For the mode $\lambda_{3,4}$, its oscillating frequency reduces while the real part moves to the imaginary axis, with the increase of SCR. However, in this condition, the damping ratio of $\lambda_{3,4}$ for both two power calculation methods are similar and generally over 0.5 at any SCR conditions, indicating that both two power calculations methods perform good damping for the mode $\lambda_{3,4}$.

Moreover, it can be found that the mode $\lambda_{1,2}$ of the virtual power method is always at the left side of the mode $\lambda_{1,2}$ of the conventional power method. This means that the virtual power method will perform better damping for the mode $\lambda_{1,2}$ if oscillating frequencies of two methods were similar. However, when the grid is weak, the oscillating frequency of the mode $\lambda_{1,2}$ of the virtual power method is a little bit larger than that of the conventional method. In this condition, the damping ratio of the mode $\lambda_{1,2}$ of the virtual power method is only slightly improved.

However, when the grid becomes stronger, the oscillating frequencies of two methods will eventually become the same. In this condition, the virtual power method will perform better damping as compared to the conventional power method. Taking condition where SCR=30 as an example, the oscillating frequencies of two methods are both around 26Hz while damping ratios of $\lambda_{1,2}$ for the conventional power method and the virtual power method are calculated around 0.04 and 0.18 respectively, which indicates better small-signal stability contributed from the virtual power calculation method.

To further investigate the small-signal stability concerning the control parameters, damping coefficient D_p is set to 40. On this basis, Fig.4 shows the dominant eigenvalues near the imaginary axis for the two methods under different SCR. In the Figure, the mode $\lambda_{1,2}$ of both two methods will move towards left with the decrease of SCR. This means that both two methods perform better damping for the mode $\lambda_{1,2}$ under the weak grid condition. For the virtual power method, the mode $\lambda_{1,2}$ is always on the left plane, indicating stability for the system. For the conventional power method, the mode $\lambda_{1,2}$ is on the left plane only when SCR is closer to 3, indicating instability under the stronger grid. Besides, when SCR=3, $\lambda_{1,2}$ of the virtual power method is more far away from the imaginary axis, indicating better damping ratio. Therefore, the virtual power method enables more stable margin and flexibility for the design of the control parameters of the GFM converter.

IV. Simulation Results

To verify the small-signal stability analysis discussed above, a single GFM converter three-phase grid-connected system is established in Matlab/Simulink. The system structure of the simulation is the same with the system structure shown in Fig.1 while and the system parameters are shown in Table I. The switching converter is modeled with its equivalent average model at the fundamental frequency, as an ideal controlled voltage source, by neglecting the high frequency switching harmonic contributions. Computational and PWM delay are considered in this condition. Besides, a 0.5Ω series resistor is connected to the filter capacitor C_f to damp the possible high frequency resonance.

Fig.5 shows the simulations results of GFM converter actual output active power with different power calculation methods under different SCR condition. It's worth noting that the actual active power of two methods shown in the figure are calculated with the same method.

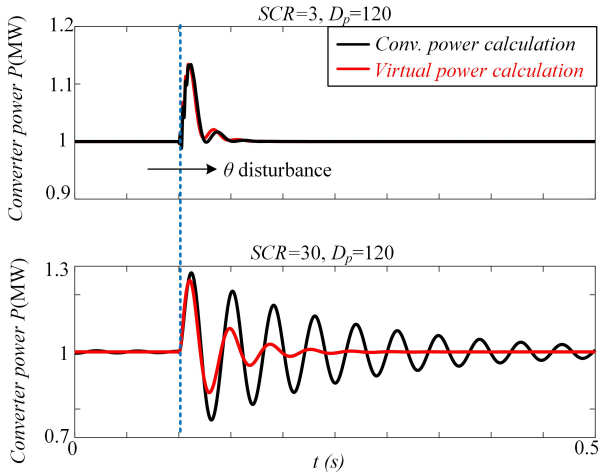

Fig. 5. Converter actual output active power under different SCR.

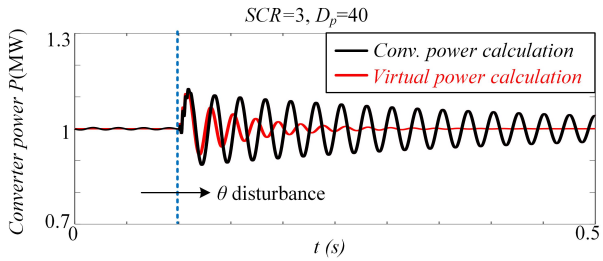

Fig. 6. Converter actual output active power under SCR=3 and D_p=40.

A small disturbance is applied to θ to excite the oscillation modes of the system. It can be found that when the SCR is set to 3, both two methods share the similar power profiles since their $\lambda_{1,2}$ are close to each other under this condition, as seen in Fig.3. When SCR is set to 30, the output power of the conventional method performs worse oscillation damping than that with the virtual power method. This is because that the mode $\lambda_{1,2}$ of the conventional power method is much more closer to the imaginary axis in this condition.

The small-signal stability is further investigated considering different damping coefficient. Fig.6 shows the simulations results of GFM converter actual output active power with different damping coefficient. In this case, the SCR is set to 3 and the damping coefficient D_p is changed from 120 to 40. Then a small disturbance is applied to θ to excite the oscillation modes of the system. It can be found that the conventional power method also performs worse damping for the mode $\lambda_{1,2}$, as compared to the virtual power method. It is worth noting that when D_p becomes lower, the mode $\lambda_{1,2}$ has worse damping ratio under the same SCR, as seen from Fig.5 and Fig.6.

TABLE I
PARAMETERS OF THE GFM CONVERTER

Symbol	Value	Symbol	Value
P^*	1 MW	Q^*	0 Var
L_1	0.1 mH	C_f	900 μF
L_g	0.05∼0.5 mH	R_g	$L_g\omega_n$/10 Ω
L_v	0.1 mH	R_v	0.1 Ω
k_p	0.12	k_i	2.5
J	0.01	D_p	120
ω_n	314 rad/s	K	50
K_f	1	K_d	0.0314
e_g	690 V (p-p rms)	SCR	3∼30

V. CONCLUSIONS

The small-signal stabilities of dual-loop VSG converter with different power calculation methods are analyzed and compared in the paper. It is found that when the conventional power calculation method is used, underdamped low frequency oscillations are more severe, especially under stronger-grid conditions. By using virtual current from the outer voltage loop to calculate the virtual power, the converter performs better damping for the low frequency oscillation mode, under both strong and weak grid condition. Simulations results are provided to validate the effectiveness of the small-signal analysis.

ACKNOWLEDGMENT

The research leading to these results was supported by Wingrid Project with funding from the European Union's Horizon 2020 research and innovation programme under the Marie Sklodowska-Curie grant agreement No 861398.

REFERENCES

[1] M. Liserre, M. A. Perez, M. Langwasser, C. A. Rojas, and Z. Zhou, "Unlocking the hidden capacity of the electrical grid through smart transformer and smart transmission," *Proceedings of the IEEE*, pp. 1–17, 2022.

[2] Z. Zhou, S. Pugliese, M. Langwasser, and M. Liserre, "Sub-synchronous damping by battery storage system in grid forming control mode," in *2022 IEEE Energy Conversion Congress and Exposition (ECCE)*, pp. 1–8, 2022.

[3] Q.-C. Zhong and G. Weiss, "Synchronverters: Inverters that mimic synchronous generators," *IEEE Transactions on Industrial Electronics*, vol. 58, no. 4, pp. 1259–1267, 2011.

[4] R. H. Lasseter, Z. Chen, and D. Pattabiraman, "Grid-forming inverters: A critical asset for the power grid," *IEEE Journal of Emerging and Selected Topics in Power Electronics*, vol. 8, no. 2, pp. 925–935, 2020.

[5] R. Rosso, X. Wang, M. Liserre, X. Lu, and S. Engelken, "Grid-forming converters: Control approaches, grid-synchronization, and future trends—a review," *IEEE Open Journal of Industry Applications*, vol. 2, pp. 93–109, 2021.

[6] P. C. Loh and D. Holmes, "Analysis of multiloop control strategies for lc/cl/lcl-filtered voltage-source and current-source inverters," *IEEE Transactions on Industry Applications*, vol. 41, no. 2, pp. 644–654, 2005.

[7] H. Wu and X. Wang, "Design-oriented transient stability analysis of grid-connected converters with power synchronization control," *IEEE Transactions on Industrial Electronics*, vol. 66, no. 8, pp. 6473–6482, 2019.

[8] Z. Kustanovich, S. Shivratri, H. Yin, F. Reissner, and G. Weiss, "Synchronverters with fast current loops," *IEEE Transactions on Industrial Electronics*, pp. 1–10, 2022.

[9] L. Huang, C. Wu, D. Zhou, and F. Blaabjerg, "Impact of virtual admittance on small-signal stability of grid-forming inverters," in *2021 6th IEEE Workshop on the Electronic Grid (eGRID)*, pp. 1–8, 2021.

APPENDIX

Small-signal differential equation of the electrical power with the conventional power calculation method is given by:

$$\begin{cases} \Delta P = \frac{3}{2}\begin{bmatrix} u_{t,d0} & u_{t,q0} \end{bmatrix}\begin{bmatrix} \Delta i_x \\ \Delta i_y \end{bmatrix} + \frac{3}{2}\begin{bmatrix} i_{d0} & i_{q0} \end{bmatrix}\begin{bmatrix} \Delta u_{t,x} \\ \Delta u_{t,y} \end{bmatrix} \\ \Delta Q = \frac{3}{2}\begin{bmatrix} u_{t,q0} & -u_{t,d0} \end{bmatrix}\begin{bmatrix} \Delta i_x \\ \Delta i_y \end{bmatrix} + \frac{3}{2}\begin{bmatrix} -i_{q0} & i_{d0} \end{bmatrix}\begin{bmatrix} \Delta u_{t,x} \\ \Delta u_{t,y} \end{bmatrix} \end{cases}. \tag{A.1}$$

Small-signal differential equation of the electrical power with the virtual power calculation method is given by:

$$\begin{cases} \Delta P_{vir} = \frac{3}{2}\begin{bmatrix} u_{t,d0} & u_{t,q0} \end{bmatrix}\begin{bmatrix} \Delta i_{vir,d} \\ \Delta i_{vir,q} \end{bmatrix} + \frac{3}{2}\begin{bmatrix} i_{vir,d0} & i_{vir,q0} \end{bmatrix}\begin{bmatrix} \Delta u_{t,x} \\ \Delta u_{t,y} \end{bmatrix} + \frac{3}{2}(i_{vir,d0}u_{t,y0} - i_{vir,q0}u_{t,x0})\Delta\theta \\ \Delta Q_{vir} = \frac{3}{2}\begin{bmatrix} u_{t,q0} & -u_{t,d0} \end{bmatrix}\begin{bmatrix} \Delta i_{vir,d} \\ \Delta i_{vir,q} \end{bmatrix} + \frac{3}{2}\begin{bmatrix} -i_{vir,q0} & i_{vir,d0} \end{bmatrix}\begin{bmatrix} \Delta u_{t,x} \\ \Delta u_{t,y} \end{bmatrix} - \frac{3}{2}(i_{vir,q0}u_{t,y0} + i_{vir,d0}u_{t,x0})\Delta\theta \end{cases}. \tag{A.2}$$

$$\mathbf{A_1} = \begin{bmatrix} \frac{-R_g}{L_g} & \omega_n & \frac{1}{L_g} & 0 & 0 & 0 & 0 & 0 & 0 & 0 & 0 & 0 & 0 \\ -\omega_n & \frac{-R_g}{L_g} & 0 & \frac{1}{L_g} & 0 & 0 & 0 & 0 & 0 & 0 & 0 & 0 & 0 \\ \frac{-1}{C_s} & 0 & 0 & \omega_n & \frac{1}{C_s} & 0 & 0 & 0 & 0 & 0 & 0 & 0 & 0 \\ 0 & \frac{-1}{C_s} & -\omega_n & 0 & 0 & \frac{1}{C_s} & 0 & 0 & 0 & 0 & 0 & 0 & 0 \\ 0 & 0 & 0 & 0 & \frac{-k_p}{L_1} & 0 & \frac{k_p}{L_1} & 0 & 0 & \frac{1}{L_1} & 0 & 0 & a_{5,13} \\ 0 & 0 & 0 & 0 & 0 & \frac{-k_p}{L_1} & 0 & \frac{k_p}{L_1} & 0 & 0 & \frac{1}{L_1} & 0 & a_{6,13} \\ 0 & 0 & \frac{-1}{L_v} & 0 & 0 & 0 & \frac{-R_v}{L_v} & \omega_n & 0 & 0 & 0 & 0 & \frac{-u_{t,y0}}{L_v} \\ 0 & 0 & 0 & \frac{-1}{L_v} & 0 & 0 & -\omega_n & \frac{-R_v}{L_v} & \frac{-1}{L_v} & 0 & 0 & 0 & \frac{u_{t,x0}}{L_v} \\ 0 & 0 & \frac{1.5i_{q0}}{K} & \frac{-1.5i_{d0}}{K} & \frac{-1.5u_{t,q0}}{K} & \frac{1.5u_{t,d0}}{K} & 0 & 0 & 0 & 0 & 0 & 0 & 0 \\ 0 & 0 & 0 & 0 & -k_i & 0 & k_i & 0 & 0 & 0 & 0 & 0 & -k_i i_{y0} \\ 0 & 0 & 0 & 0 & 0 & -k_i & 0 & k_i & 0 & 0 & 0 & 0 & k_i i_{x0} \\ 0 & 0 & \frac{-1.5i_{d0}}{J\omega_n} & \frac{-1.5i_{q0}}{J\omega_n} & \frac{-1.5u_{t,d0}}{J\omega_n} & \frac{-1.5u_{t,q0}}{J\omega_n} & 0 & 0 & 0 & 0 & 0 & \frac{-D_p}{J} & 0 \\ 0 & 0 & 0 & 0 & 0 & 0 & 0 & 0 & 0 & 0 & 0 & 1 & 0 \end{bmatrix} \tag{A.3}$$

where $a_{5,13} = (\omega_n L_1 i_{x0} + u_{t,y0} - k_p i_{y0} - u_{c,q0})/L_1$ and $a_{6,13} = (\omega_n L_1 i_{y0} - u_{t,x0} + k_p i_{x0} + u_{c,d0})/L_1$.

$$\mathbf{A}_2 = \begin{bmatrix} \frac{-R_g}{L_g} & \omega_n & \frac{1}{L_g} & 0 & 0 & 0 & 0 & 0 & 0 & 0 & 0 & 0 & 0 \\ -\omega_n & \frac{-R_g}{L_g} & 0 & \frac{1}{L_g} & 0 & 0 & 0 & 0 & 0 & 0 & 0 & 0 & 0 \\ \frac{-1}{C_s} & 0 & 0 & \omega_n & \frac{1}{C_s} & 0 & 0 & 0 & 0 & 0 & 0 & 0 & 0 \\ 0 & \frac{-1}{C_s} & -\omega_n & 0 & 0 & \frac{1}{C_s} & 0 & 0 & 0 & 0 & 0 & 0 & 0 \\ 0 & 0 & 0 & 0 & \frac{-k_p}{L_1} & 0 & \frac{k_p}{L_1} & 0 & 0 & \frac{1}{L_1} & 0 & 0 & a_{5,13} \\ 0 & 0 & 0 & 0 & 0 & \frac{-k_p}{L_1} & 0 & \frac{k_p}{L_1} & 0 & 0 & \frac{1}{L_1} & 0 & a_{6,13} \\ 0 & 0 & \frac{-1}{L_v} & 0 & 0 & 0 & \frac{-R_v}{L_v} & \omega_n & 0 & 0 & 0 & 0 & \frac{-u_{t,y0}}{L_v} \\ 0 & 0 & 0 & \frac{-1}{L_v} & 0 & 0 & -\omega_n & \frac{-R_v}{L_v} & \frac{-1}{L_v} & 0 & 0 & 0 & \frac{u_{t,x0}}{L_v} \\ 0 & 0 & \frac{1.5i_{v,q0}}{K} & \frac{-1.5i_{v,d0}}{K} & 0 & 0 & \frac{-1.5u_{t,q0}}{K} & \frac{1.5u_{t,d0}}{K} & 0 & 0 & 0 & 0 & a_{9,13} \\ 0 & 0 & 0 & 0 & -k_i & 0 & k_i & 0 & 0 & 0 & 0 & 0 & -k_i i_{y0} \\ 0 & 0 & 0 & 0 & 0 & -k_i & 0 & k_i & 0 & 0 & 0 & 0 & k_i i_{x0} \\ 0 & 0 & \frac{-1.5i_{vir,d0}}{J\omega_n} & \frac{-1.5i_{vir,q0}}{J\omega_n} & 0 & 0 & \frac{-1.5u_{t,d0}}{J\omega_n} & \frac{-1.5u_{t,q0}}{J\omega_n} & 0 & 0 & 0 & \frac{-D_p}{J} & a_{12,13} \\ 0 & 0 & 0 & 0 & 0 & 0 & 0 & 0 & 0 & 0 & 0 & 1 & 0 \end{bmatrix} \tag{A.4}$$

where $a_{9,13} = 1.5(i_{vir,q0}u_{t,y0} + i_{vir,d0}u_{t,x0})/K$ and $a_{12,13} = 1.5(i_{vir,q0}u_{t,x0} - i_{vir,d0}u_{t,y0})/(J\omega_n)$.